Downloaded from https://academic.oup.com/mnras/article/540/3/2820/8154498 by University of Southampton user on 13 August 2025

# Long time-scale numerical simulations of large supercritical accretion discs

P. Chris Fragile <sup>10</sup>, 1,2★ Matthew J. Middleton, Deepika A. Bollimpalli <sup>10</sup> and Zach Smith

Accepted 2025 May 28. Received 2025 May 13; in original form 2025 February 13

#### ABSTRACT

In this paper, we report on three of the largest (in terms of simulation domain size) and longest (in terms of duration) 3D general relativistic radiation magnetohydrodynamic simulations of supercritical accretion on to black holes. The simulations are all set for a rapidly rotating ( $a_* = 0.9$ ) stellar-mass ( $M_{\rm BH} = 6.62 M_{\odot}$ ) black hole. The simulations vary in their initial target mass accretion rates (assumed measured at large radius), with values sampled in the range  $\dot{m} = \dot{M}/\dot{M}_{\rm Edd} = 1$ –10. We find in practice, though, that all of our simulations settle close to a net accretion rate of  $\dot{m}_{\rm net} = \dot{m}_{\rm in} - \dot{m}_{\rm out} \approx 1$  (over the radii where our simulations have reached equilibrium), even though the inward mass flux (measured at large radii)  $\dot{m}_{\rm in}$  can exceed 1000 in some cases. This is possible because the outflowing mass flux  $\dot{m}_{\rm out}$  adjusts itself to very nearly cancel out  $\dot{m}_{\rm in}$ , so that at all radii  $\dot{M}_{\rm net} \approx \dot{M}_{\rm Edd}$ . In other words, these simulated discs obey the Eddington limit. We compare our results with the predictions of the slim disc (advection-dominated) and critical disc (wind/outflow-dominated) models, finding that they agree quite well with the critical disc model both qualitatively and quantitatively. We also speculate as to why our results appear to contradict most previous numerical studies of supercritical accretion.

**Key words:** accretion, accretion discs – radiation: dynamics – stars: black holes – X-rays: binaries.

### 1 INTRODUCTION

Supercritical accretion, where mass is fed into a system above the nominal Eddington limit, plays a crucial role in many astrophysical settings. It may be a factor in the formation of the first supermassive black holes (Volonteri & Rees 2005; Schneider et al. 2023; Bennett et al. 2024); it likely governs the early evolution of tidal disruption events (TDEs; Dai et al. 2018; Wu, Coughlin & Nixon 2018); and it is important for understanding the observational appearance of ultraluminous X-ray sources (ULXs; King et al. 2001; Kaaret, Feng & Roberts 2017; King, Lasota & Middleton 2023).

The Eddington limit is defined as the state in which there is a perfect balance between the gravitational force attracting matter to a central object and the outward radiation force coming from that object. Assuming an electron-scattering opacity, a pure hydrogen composition, and spherical symmetry gives the standard expression

$$L_{\rm Edd} = \frac{4\pi G M_{\rm BH} m_{\rm p} c}{\sigma_T} = 1.3 \times 10^{38} \left(\frac{M_{\rm BH}}{M_{\odot}}\right) {\rm erg \ s^{-1}} \ .$$
 (1)

If we assume the luminosity is powered by accretion on to a black hole, then it is common to take  $L_{\rm Edd} = \eta \dot{M}_{\rm Edd} c^2$ , where  $\dot{M}_{\rm Edd}$  is the corresponding Eddington mass accretion rate and  $\eta$  is the radiative efficiency of the disc.

Supercritical accretion has been widely studied, both from an observational perspective and theoretically (see Kaaret et al. 2017;

King et al. 2023, and references therein). The fundamental issue with supercritical accretion is that, if all the gravitational binding energy of the accreting matter were liberated locally in the form of radiation, as in the standard disc model, then the radiative forces would exceed the gravitational ones, and the disc cannot be in balance. Broadly speaking, two classes of solutions have been proposed to address this problem. The first posits that not all of the energy is actually radiated locally; instead, some of it is advected into the black hole before it has time to escape. The most popular solution within this class is the so-called 'slim' disc (Abramowicz et al. 1988; Beloborodov 1998; Sadowski 2009). In the second class of solutions, the excess liberated energy is used to drive an outflow, effectively limiting the amount of matter that actually accretes to smaller radii (Shakura & Sunyaev 1973). One example of a solution in this class is the 'critical' disc (Fukue 2004). There are also models that combine some degree of advection and outflow (Fukue 2004; Poutanen et al. 2007).

Supercritical accretion has also been studied numerically (e.g. Ohsuga et al. 2005; Jiang, Stone & Davis 2014; Sądowski & Narayan 2016; Takahashi, Mineshige & Ohsuga 2018; Asahina & Ohsuga 2022; Utsumi et al. 2022). However, all previous numerical studies differ from the work we present in one or more crucial aspects. For instance, many studies were performed in two-dimensions using an explicit viscosity (e.g. Ohsuga et al. 2005; Kitaki et al. 2021; Hu et al. 2022; Yoshioka et al. 2022). Such simulations preclude

<sup>&</sup>lt;sup>1</sup>Department of Physics and Astronomy, College of Charleston, 66 George Street, Charleston, SC 29424, USA

<sup>&</sup>lt;sup>2</sup>Department of Physics and Astronomy, University of Southampton, Highfield, Southampton SO17 1BJ, UK

<sup>&</sup>lt;sup>3</sup>Department of Astronomy, Astrophysics and Space Engineering, Indian Institute of Technology Indore, Simrol 453552, Indore, Madhya Pradesh, India

<sup>\*</sup> E-mail: fragilep@cofc.edu

<sup>&</sup>lt;sup>1</sup>Note that for accreting objects that have physical surfaces, such as neutron stars, all of the liberated accretion energy must ultimately escape.

any magnetohydrodynamic (MHD) turbulence, magnetically driven outflows, and any non-axisymmetric effects. Others were initialized with a finite torus of gas (e.g. Jiang et al. 2014; Sądowski & Narayan 2016; Utsumi et al. 2022). Such simulations can never truly achieve a global steady state, as the mass reservoir is continuously depleted. More importantly, most of these simulations started with tori that were smaller than their corresponding trapping radius  $r_{\rm tr} \sim \dot{m}_{\rm BH} r_g$ , where  $r_g = G M_{\rm BH}/c^2$  is the gravitational radius and  $\dot{m}_{\rm BH}$  is the mass feeding rate measured at the black hole, possibly forcing them to favour the advective, rather than outflow, solution (Kitaki et al. 2021; Yoshioka et al. 2022). Since our simulations correct many of these issues, we feel they offer an important new perspective in the study of supercritical accretion.

Since our work focuses on large steady-state accretion discs, the results are probably most applicable to the case of ULXs. TDEs likely have relatively small discs with rapidly varying mass accretion rates, whereas ULXs have comparatively large discs and more stable accretion rates (although see Middleton et al. 2022). The numerical simulations reported in this paper have been specifically designed to match the latter conditions.

In this paper, we first describe our numerical set-up (Section 2), then highlight results regarding the actual feeding rate of material on to the black hole, as well as the luminosity of the disc (Section 3). We also compare our results to the two broad classes of supercritical accretion models (Section 4) and compare our results with previous numerical studies (Section 5). We end with our concluding thoughts (Section 6).

### 2 NUMERICAL SET-UP

All of our simulations are performed using the general relativistic radiation MHD (GRRMHD) code Cosmos++ (Anninos, Fragile & Salmonson 2005). We use high-resolution shock-capturing (Fragile et al. 2012) to solve for the flux and gravitational source terms of the gas and radiation; for the magnetic fields, we evolve the magnetic vector potential (Fragile et al. 2019); and for the radiation, we use the (grey opacity) M<sub>1</sub> closure scheme (Fragile, Olejar & Anninos 2014). Together, these allow us to evolve the following 12 conserved fields: the fluid density  $D = W \rho$ , the fluid total energy density  $\mathcal{E} = -\sqrt{-g}T_0^0$ , the fluid momentum density  $\mathcal{S}_j = \sqrt{-g}T_j^0$ , the magnetic vector potential  $A_i$ , the radiation total energy density  $\mathcal{R} = \sqrt{-g}R_0^0$ , and the radiation momentum density  $\mathcal{R}_i = \sqrt{-g}R_i^0$ where  $W = \sqrt{-g}u^t$  is the generalized boost factor, g is the fourmetric determinant,  $\rho$  is the rest-mass density,  $u^{\mu}$  is the fluid fourvelocity,  $T^{\mu\nu}$  is the fluid stress-energy tensor, and  $R^{\mu\nu}$  is the radiation stress-energy tensor. The fluid and radiation fields are coupled through the radiation four-force density

$$G^{\mu} = -\rho(\kappa_F^a + \kappa^s)R^{\mu\nu}u_{\nu} \tag{2}$$

$$-\rho \left\{ \left[ \kappa^s + 4\kappa^s \left( \frac{T_{\text{gas}} - T_{\text{rad}}}{m_e} \right) + \kappa_F^a - \kappa_J^a \right] \right\}$$
 (3)

$$\times R^{\alpha\beta}u_{\alpha}u_{\beta} + \kappa_{\rm p}^{\rm a}a_{R}T_{\rm gas}^{4} \right\} u^{\mu} , \qquad (4)$$

where we assume Planck and Rosseland mean opacities  $\kappa_{\rm P}^a=2.8\times 10^{23}\,T_{\rm K}^{-7/2}\rho_{\rm cgs}$  cm² g<sup>-1</sup> and  $\kappa_{\rm R}^a=7.6\times 10^{21}\,T_{\rm K}^{-7/2}\,\rho_{\rm cgs}$  cm² g<sup>-1</sup>, respectively, and  $\kappa^{\rm s}=0.34$  cm² g<sup>-1</sup> for the scattering opacity, appropriate for solar metallicity with mean molecular weight  $\mu=$ 

0.615 and a hydrogen-mass fraction of X = 0.7. We use the 9D numerical inversion scheme with analytic derivatives from Fragile et al. (2014) to recover the primitive fluid and radiation fields. The necessary magnetic field components, including the face-centred conserved fields  $\mathcal{B}^i$  and zone-centred primitive field  $\mathcal{B}^i$ , are recovered from the updated vector potential (Fragile et al. 2019).

To initialize our simulations, we start from the Novikov & Thorne (1973) generalization of the Shakura–Sunyaev (Shakura & Sunyaev 1973) thin disc. As we are only considering a limited radial range, we do not require all three regions of the solution. Instead, we only initialize the so-called 'inner' (radiation-pressure-dominated) region, which should exist out to  $r \ge 100r_g$  at the accretion rates we are considering. We follow the form of the Novikov-Thorne solutions given in Abramowicz & Fragile (2013). This simply requires us to choose a mass for the black hole  $M_{\rm BH}$ , a target mass feeding rate  $\dot{m}_0$ measured at large radius, and a Shakura-Sunyaev viscosity parameter  $\alpha_{\rm SS}$  for the disc. We choose  $\alpha_{\rm SS}=0.02$  for our initial set-up, though it is difficult to specify a priori what value we should use, as there are multiple possible sources of angular momentum transport in our simulations (MHD turbulence and magnetically driven winds), and we cannot know ahead of time what effective  $\alpha$  they will lead to. Ultimately, however, our goal is just to begin the simulations from some reasonable initial conditions that cover a large radial range. As explained later, we then give the discs plenty of time to approach their true solutions.

From the Novikov–Thorne solution, all we actually require are the radial dependencies of the height H(R) and mid-plane density  $\rho_0(R)$  of the disc.<sup>3</sup> We also include a small radial velocity  $V^R(R)$ , associated with the slow inward drift of material through the disc (Penna, Sądowski & McKinney 2012). The initial azimuthal velocity is taken to be Keplerian,  $V^\phi(R) = \Omega = (M_{\rm BH}/R^3)^{1/2} \left[1 + a_*(M_{\rm BH}/R^3)^{1/2}\right]^{-1}$ .

For the vertical profile, we solve for hydrostatic equilibrium assuming a polytropic equation of state with  $\Gamma_{NT}=4/3$ . The solution yields

$$\rho(R,z) = \rho_0 \left[ 1 - \frac{z^2}{2H^2} \right]^{1/(\Gamma_{NT} - 1)}$$
 (5)

and

$$P_{\text{tot}}(R, z) = \kappa \rho^{\Gamma_{\text{NT}}} , \qquad (6)$$

where

$$\kappa = \frac{GM_{\rm BH}H^2}{\Gamma_{\rm NT}(\Gamma_{\rm NT} - 1)\rho_0^{\Gamma_{\rm NT} - 1}R^3} \ . \tag{7}$$

For the background, we initialize a cold  $(e=3\times 10^{-6}e_{\rm max}r^{-2})$  low density  $(\rho=10^{-4}\rho_{\rm max}r^{-3/2})$  free-falling  $(u^r=-\sqrt{r_{\rm BH}/r})$  fluid, where  $r_{\rm BH}=\left(1+\sqrt{1-a_*^2}\right)r_g$  is the radius of the black hole and  $a_*$  is its dimensionless spin.

Assuming the gas and radiation are in local thermodynamic equilibrium inside the disc for the initial, analytic solution, we partition the pressure as

$$P_{\text{tot}} = P_{\text{gas}} + P_{\text{rad}} = \frac{k_{\text{b}}\rho T_{\text{gas}}}{\bar{m}} + \frac{1}{3}a_{\text{R}}T_{\text{gas}}^{4},$$
 (8)

where  $\bar{m} = \mu m_H$  and  $a_R = 4\sigma_B/c$  is the radiation constant. We can now solve this quartic equation for  $T_{\rm gas}(R,z)$ . This temperature is

<sup>&</sup>lt;sup>2</sup>Throughout this paper,  $\dot{m}$  refers to mass accretion rates scaled to Eddington, i.e.  $\dot{m} = \dot{M}/\dot{M}_{\rm Edd}$ .

<sup>&</sup>lt;sup>3</sup>We take r as the spherical-polar radius and  $R = r \sin \theta$  as the cylindrical one.

also used to set the initial radiation field. In the frame of the fluid, the radiation energy density is taken to be

$$E_{\rm rad} = a_R T_{\rm gas}^4 \,, \tag{9}$$

while the flux,  $F^i$ , is initially set equal to the gradient of this quantity. To get the radiation density in the radiation rest frame,  $E_R$ , and the radiation rest-frame four-velocity,  $u_R^{\mu}$ , we follow the transformation procedure outlined in Sądowski et al. (2013).

One issue with the inner region of the Shakura–Sunyaev thin-disc solution is that it is thermally unstable (Shakura & Sunyaev 1976), as confirmed in earlier numerical work (Jiang et al. 2013; Mishra et al. 2016; Fragile et al. 2018). One mechanism that can stabilize such discs is the introduction of strong (particularly, toroidal) magnetic fields (Begelman & Pringle 2007), which require particular global magnetic field topologies to maintain (Sądowski 2016; Mishra et al. 2022). The present simulations start from one such configuration: a zero-net-flux quadrupole field that has two poloidal field loops of opposite polarity stacked vertically, one on top of the other, about the mid-plane of the disc. The two poloidal loops are greatly elongated in the radial direction, extending from near the inner radius of the disc to nearly the outer boundary of our simulation domain. To initialize this field, we first set the azimuthal component of the vector potential

$$A_{\phi} \propto R^{1.5} z \frac{\sqrt{e^{(-2.5z^2/H^2)}} \sin{(\pi R/r_{\text{max}})}}{1 + e^{\Delta}} ,$$
 (10)

where  $r_{\text{max}}$  is the maximum radius of the grid, and

$$\Delta = 10 \left( \frac{z^2}{H^2} + \frac{(R - R_t)^2}{H^2} - 1 \right) , \tag{11}$$

where  $R_t = \max(r_{\rm ISCO}, R)$ , and  $r_{\rm ISCO}$  is the usual innermost stable circular orbit radius. We then set the poloidal components of the magnetic field as  $\mathcal{B}^r = -\partial_\theta A_\phi$  and  $\mathcal{B}^\theta = \partial_r A_\phi$ . These choices keep the initial magnetic field divergence-free and confined within the initial disc. This particular field configuration is subject to a strong radial shear amplification (leading to a growth of the  $\mathcal{B}^\phi$  component) due to the orbital motion of the disc (the so-called  $\Omega$ -dynamo). Along with the normal magnetorotational-instability (MRI)-driven amplification, this has been shown to help stabilize similar discs against thermal instability (Sądowski 2016; Mishra et al. 2022).

The simulations are run on a nested (statically refined) spherical-polar grid with resolution concentrated near the black hole and towards the mid-plane. We use a logarithmic radial coordinate,  $x_1 = 1 + \ln(r/r_{\rm BH})$ , to cover the range from  $0.9\,r_{\rm BH} \le r \lesssim 1000\,r_g$ . As such, these are the largest three-dimensional supercritical accretion simulations in terms of the size of the disc that we are aware of, comparable to earlier large-domain two-dimensional simulations (Kitaki et al. 2021; Yoshioka et al. 2022). The advantage of using such large discs and starting from a Shakura–Sunyaev solution instead of a finite torus is that the simulations can be run for very long times with nearly steady mass accretion rates. It also gives us an opportunity to capture the critical radius, given analytically by (Fukue 2004; Poutanen et al. 2007):

$$r_{\rm cr} \approx \frac{5}{3}\dot{m}_0,\tag{12}$$

on the grid, which is the radius inside of which the radiative forces overcome gravity and the traditional disc solution is no longer valid. This has not been the case in most previous numerical work (see Kitaki et al. 2021). We include the full polar  $(0 \le \theta \le \pi)$  and azimuthal  $(0 \le \phi \le 2\pi)$  domains. To improve the resolution near the mid-plane, a concentrated polar coordinate,  $\theta = x_2 + h \sin(2x_2)$ ,

is used. The base mesh has a resolution of  $48 \times 32 \times 24$  zones in  $\{x_1, x_2, \phi\}$ . Outflow boundary conditions are applied at the inner and outer radial limits of the domain, while transmissive boundaries are applied at the poles and periodic boundaries are used in  $\phi$ .

As mentioned before, we already know that the Shakura-Sunyaev disc solution is invalid once the mass accretion rate exceeds Eddington, so another option would have been to start our simulations with one of the supercritical disc solutions proposed in Section 1. However, since one of our goals is to assess which class of supercritical solution is applicable to large steady-state discs, we choose, instead, to start from the Shakura-Sunyaev solution and simply give our discs sufficient time to find their preferred supercritical states. To do this in a computationally efficient way, we start all of our simulations on a very low resolution, two-level mesh (base mesh plus one refinement layer for an effective resolution of  $96 \times 64 \times 48$ ) and allow them to run to  $t_{\text{stop}} \gtrsim 70\,000\,t_g$ , where  $t_g = GM/c^3$ . This is longer than the thermal time-scale of the disc  $(t_{\rm th} \sim [\alpha \Omega]^{-1})$  out to  $r \gtrsim 150 \, r_g$ and the accretion time-scale  $(t_{acc} \sim r/|V^r|)$  out to  $r \gtrsim 20 r_g$ . After this initial 'burn-in' period, we increase the resolution in one of our simulations by adding another refinement layer before running it for an additional 15 000  $t_g$ . A plot of this high-resolution disc and grid is shown in Fig. 1.

The modest resolutions of our two-level meshes mean that we are not formally resolving the MRI (quality factors  $Q_i = \lambda_{\text{MRI},i}/\Delta x_i$  of  $Q_{\theta} \approx 1$  and  $Q_{\phi} \approx 4$ , respectively, where  $\lambda_{\text{MRI},i} = 2\pi v_{A,i}/|V^{\phi}|$  is the wavelength of fastest growing MRI mode,  $\Delta x_i$  is a typical zone length, and  $v_{A,i} = \sqrt{b^i b_i / \rho}$  is Alfvén speed in directions  $i = \{\theta, \phi\}$ ). This may lead to our relatively low values for  $\alpha \equiv \langle W_{\hat{r}\hat{\phi}}/P_{\text{tot}}\rangle_t$ of  $10^{-3}$ – $10^{-2}$ . However, one has to be careful here. First, we are not using the typical set-up of a dipole magnetic field inside a finite torus that has been carefully studied and from which the 'standard' Q values are mostly derived (Hawley, Guan & Krolik 2011; Hawley et al. 2013). In fact, for our configuration, with a vertically stacked quadrupole field, there is very little  $\mathcal{B}^{\theta}$  to be found in the bulk of the disc. This means our simulations are probably less reliant on the typical axisymmetric modes of the MRI and more dependent on the non-axisymmetric ones, which have been far less studied in terms of saturation values and resolution requirements. Furthermore, with regard to  $Q_{\phi}$ , there are two current sheets that form in our simulations, one a little above the midplane and another a little below; this is in contrast to the single current sheet associated with the standard dipole field. This means there will also be regions with relatively weak  $\mathcal{B}^{\phi}$  fields. Finally, since much of the angular momentum transport in these discs is likely in the form of winds, it is unclear how critical the MRI actually is. Additional work will be needed to clarify all of these issues.

In this paper, we report three simulations that vary in their nominal, or intended, mass accretion rate  $\dot{m}_0 = \dot{M}/\dot{M}_{\rm Edd}$  (assumed measured at large radius), their maximum radial extent  $r_{\rm max}$ , and angular concentration parameter h, as detailed in Table 1. In all other respects, the simulations are the same, with  $M_{\rm BH}=6.62{\rm M}_{\odot}$  and  $a_*=0.9$  ( $\eta_{\rm NT}=0.156$ ).

### 3 RESULTS

### 3.1 Mass accretion

### 3.1.1 Black hole growth rates

If the mass accretion rate  $\dot{M}$  is assumed constant throughout, such that the mass accretion rate on to the black hole equals whatever

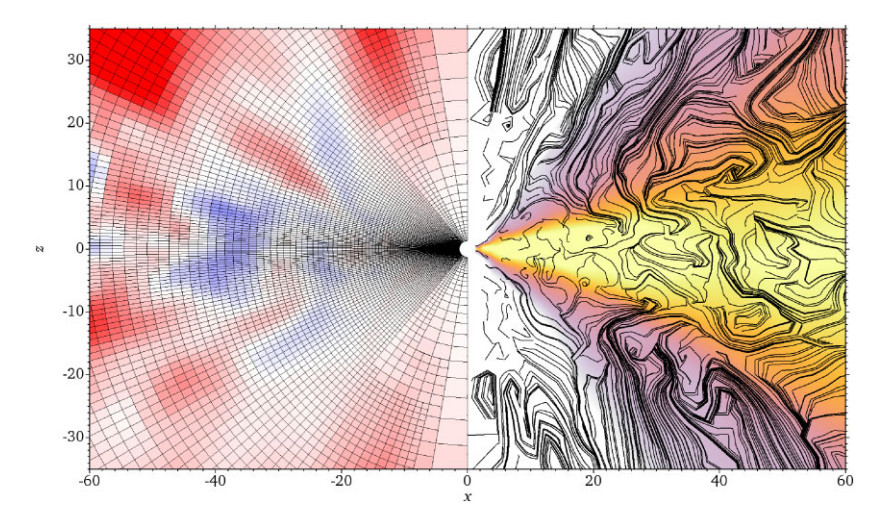


**Figure 1.** Disc and grid configuration at the start of a9r20L3 (the high-resolution interval for simulation a9r20). The *left* panel shows the statically refined grid, as well as the radiative flux (arbitrary units). The red colours indicate outgoing flux, while the blue colours indicate flux moving towards the black hole. The *right* panel shows the logarithm of the gas density, covering three orders of magnitude, as well as magnetic field streamlines launched from a uniform sample of points in the plane of this slice.

**Table 1.** Simulation models and parameters.

|       | $\dot{m}_0$ | $r_{\rm max}/r_g$ | h    | $t_{\rm stop}/t_g$ | $r_{\rm eq}/r_g$ | $\langle \dot{m}_{\rm in}(r_{\rm eq}) \rangle_t$ | $\langle \dot{m}_{ m BH}  angle_t$ | $\frac{\langle L_{\rm out}(r_{\rm eq})\rangle_t}{L_{\rm Edd}}$ | $\frac{\langle L_{\rm kin}(r_{\rm eq})\rangle_t}{L_{\rm Edd}}$ | $\langle \eta  angle_t$ |
|-------|-------------|-------------------|------|--------------------|------------------|--|------------------------------------|--|--|-------------------------|
| a9r5  | 1           | 300               | 0.12 | 71 625             | 32               | 67   | 1.8                                | ≤ 6.3  | ≤ 6.4  | ≤ 0.5                   |
| a9r20 | 4           | 1000              | 0.35 | 165 771            | 49               | 42   | 1.2                                | $\leq 5.0$   | $\leq 2.6$   | $\leq 0.7$              |
| a9r50 | 10          | 1000              | 0.35 | 100 000            | 32               | 23   | 1.9                                | $\leq 3.8$   | ≤ 1.6  | $\leq 0.4$              |

value is fed in at the outer edge of the disc  $\dot{M}_0$ , then the black hole mass will grow linearly as

$$M_{\rm BH}(t) = M_{\rm BH}(t_0) + \dot{M}_0 t ,$$
 (13)

where  $M_{\rm BH}(t_0)$  is the initial mass, and the growth time will be  $\tau_{\rm grow} = M_{\rm BH}(t_0)/\dot{M}_0$ . However, whenever the mass-accretion rate at the outer edge exceeds the Eddington rate, accretion at the inner edge is expected to be suppressed to

$$\dot{M}_{\rm BH} \approx \dot{M}_{\rm Edd} \,, \tag{14}$$

and the black hole mass grows exponentially as

$$M_{\rm BH}(t) = M_{\rm BH}(t_0)e^{t/\tau_{\rm grow}} , \qquad (15)$$

where the growth time is now  $\tau_{\rm grow} \approx M_{\rm BH}(t_0)/\dot{M}_{\rm Edd}$ . Numerically, this corresponds to  $\tau_{\rm grow} \approx 4.4 \times 10^8 \, \eta$  yr in the super-Eddington case, which leads to difficulties when trying to understand how black holes can reach masses of up to  $10^9 M_{\odot}$  by the time the Universe was < 700 Myr old (Bañados et al. 2018; Yang et al. 2021). So, our first goal with our supercritical simulations is to confirm whether the mass accretion rate on to the black hole really is limited.

In Fig. 2, we report the time history of mass accretion on to the black hole

$$\dot{M}_{\rm BH}(r_{\rm BH},t) = -\int \int \sqrt{-g} \rho u^r \, \mathrm{d}\theta \, \mathrm{d}\phi \tag{16}$$

for all three simulations. The remarkable finding is that they all produce mass accretion rates on to the black hole within a factor of 3 of  $\dot{M}_{\rm Edd}$  despite covering a full order of magnitude difference in their target value  $\dot{m}_0$ . The  $\dot{m}_{\rm BH}$  values are also remarkably steady over time, though there is some evidence for slow secular trends towards increasing  $\dot{m}_{\rm BH}$  lasting at least  $70\,000\,t_g$  in all three cases.

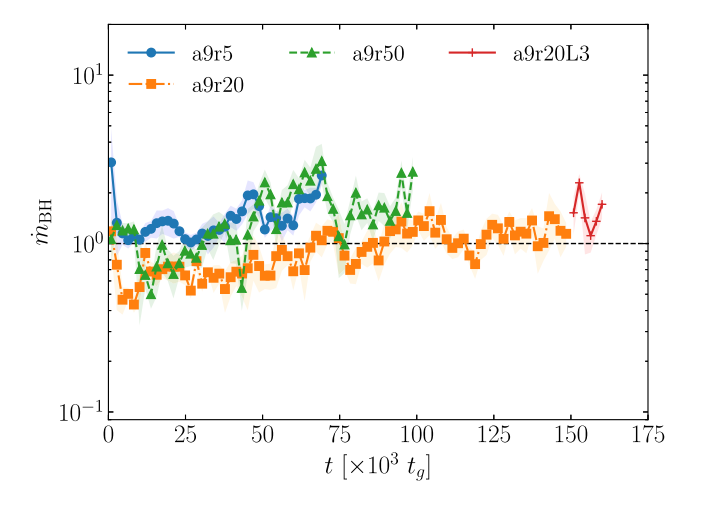


**Figure 2.** Mass accretion rate through the black hole event horizon in units of the Eddington accretion rate  $\dot{m}_{\rm BH} = \dot{M}_{\rm BH}/\dot{M}_{\rm Edd}$ , smoothed using moving averages over 20 consecutive dumps ( $\approx 1850\,t_g$  in time). The shaded regions show the  $1\sigma$  standard deviations, and the black dashed line shows the Eddington limit.

Additionally, there is maybe a slight jump up in  $\dot{m}_{\rm BH}$  whenever we increase the resolution of our a9r20 simulation.<sup>4</sup> Still, the clustering of our results around  $\dot{m}_{\rm BH} \approx 1$  is noteworthy.

<sup>&</sup>lt;sup>4</sup>Throughout this paper, we refer to the high-resolution extension of simulation a9r20 as a9r20L3.

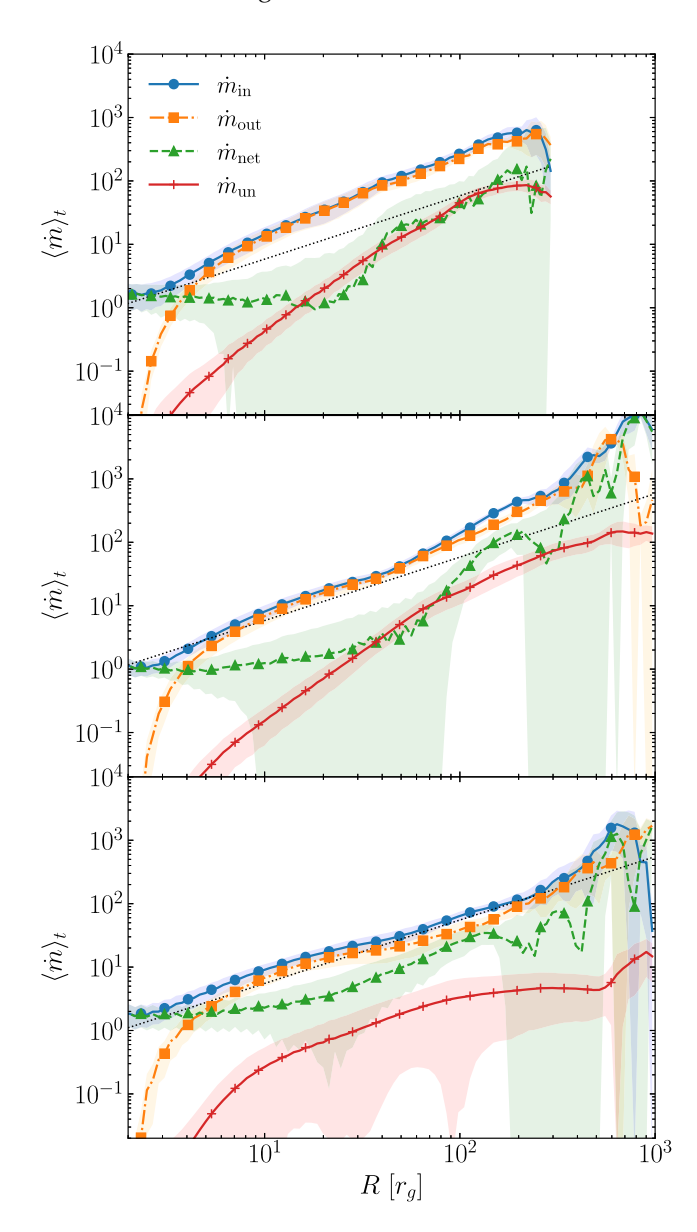


**Figure 3.** Mass fluxes, both inward  $(\dot{m}_{\rm in})$  and outward  $(\dot{m}_{\rm out})$ , as well as the net mass flux  $\dot{m}_{\rm net} = \dot{m}_{\rm in} - \dot{m}_{\rm out}$ , all scaled to Eddington and time averaged from  $t = 50\,000\,t_g$  or  $100\,000\,t_g$  to  $t_{\rm stop}$  for the a9r5 (top), a9r20 (middle), and a9r50 (bottom) simulations. The other curves report the portion of  $\dot{m}_{\rm out}$  that has a positive Bernoulli parameter  $(\dot{m}_{\rm un})$  and an analytic estimate for  $\dot{m}_{\rm in}(r) = [\dot{m}_{\rm in}(r_{\rm cr}) - \dot{m}_{\rm BH}]r/r_{\rm cr}$  (black, dotted curve). The shaded regions show  $1\sigma$  standard deviations.

### 3.1.2 How the Eddington limit is achieved

It is very instructive to see how each of these simulations achieves these nearly identical values of  $\dot{m}_{\rm BH}$ . Fig. 3 shows time-averaged radial profiles of mass flux, both inwards

$$\dot{M}_{\rm in}(r,t) = -\int \int \sqrt{-g}\rho \min\{u^r, 0\} \mathrm{d}\theta \,\mathrm{d}\phi \tag{17}$$

and outwards

$$\dot{M}_{\text{out}}(r,t) = \int \int \sqrt{-g} \rho \max\{u^r, 0\} d\theta d\phi , \qquad (18)$$

for all three simulations. These data are time averaged from  $t = 50\,000\,t_g$  until  $t_{\text{stop}}$  for simulations a9r5 and a9r50 and from  $t = 100\,000\,t_g$  until  $t_{\text{stop}}$  for simulation a9r20. We also plot  $\dot{M}_{\text{net}} = \dot{M}_{\text{in}} -$ 

 $\dot{M}_{\rm out}$ , which is an important quantity, as in a steady state, this should be constant as a function of radius (regardless of what supercritical disc model applies). Thus, we can see from Fig. 3 that we have achieved a reasonably steady state out to  $\gtrsim 30r_g$  in all three cases. Lastly, Fig. 3 includes  $\dot{M}_{\rm un}$ , which represents the portion of  $\dot{M}_{\rm out}$ that has a positive Bernoulli parameter  $Be = -(T_t^t + R_t^t + \rho u^t) > 0$ (Sadowski & Narayan 2016) and thus is likely to be unbound and ultimately escape to infinity. The fact that  $\dot{m}_{\rm out}$  significantly exceeds  $\dot{m}_{\rm un}$  in Fig. 3 implies that much of the material moving outwards on our computational domain may eventually turn around and fall back towards the black hole. However, using the Bernoulli parameter to define the unbound outflow is a fairly conservative estimate, as it is possible for matter to be launched with a negative Be, yet receive additional acceleration and ultimately escape (Yoshioka et al. 2022). As this does not happen within our computational domain, the ultimate fate of this material remains uncertain. As a final note on how these quantities are measured, we emphasize that the mass outflow rates ( $\dot{M}_{\rm out}$  and  $\dot{M}_{\rm un}$ ) are cumulative; in other words, at any given radius they could include matter launched from that or any interior radius. They simply report how much mass is moving outwards through a given radius at a given time, irrespective of where it launched from.

An important takeaway from Fig. 3 is that  $\dot{m}_{\rm in}$  and  $\dot{m}_{\rm net}$  both approach 1 at the inner boundary of the computational domain (i.e. at the black hole event horizon). This is achieved despite the fact that  $\dot{m}_{\rm in}$  can be quite large (easily > 100) at large radius. This is possible because the mass outflow  $\dot{m}_{\rm out}$  carefully balances the inflow (compare the blue and orange curves in each panel). In fact, the magnitudes of  $\dot{m}_{\rm in}$  and  $\dot{m}_{\rm out}$  are so large and the balance so finely tuned that the difference between the two,  $\dot{m}_{\rm net}$ , shows large statistical fluctuations, particularly on the low side, since it often changes sign (explaining the large green shaded regions in the top two panels of the figure).

Table 1 reports values for  $\langle \dot{m}_{\rm BH} \rangle_t$ , the time-averaged mass accretion rates on to the black hole for each simulation. These results strongly suggest that  $\dot{M}_{\rm Edd}$  is a meaningful limit for these simulations, and the discs adjust as necessary to meet it. As mentioned previously, this could have major implications for the growth of supermassive black holes in the very early Universe. It is also a somewhat surprising result in that it disagrees with practically all previous numerical simulations of supercritical accretion, a point we return to in Section 5.

The reader may wonder how the inward mass accretion rates in Fig. 3 can exceed our reported values for  $\dot{m}_0$  by an order of magnitude or more at large radii. First, it may help to emphasize that each  $\dot{m}(r)$  comes from an integral over a full  $4\pi$  sr shell. So, especially in the outer disc where there is a lot of mass, if the disc simply sloshes around, it will appear as very large values of  $\dot{m}$  (both inward and outward). Additionally, since none of our simulations have reached steady-state solutions at large radii, what we are seeing there may prove to just be an unfortunate transient state set up by our imperfect initial conditions. However, we find it reassuring that the total mass within our computational domain drops by less than 8 per cent even in our longest duration simulation, so despite what appear to be very large fluxes, we are not actually gaining or losing that much mass compared to what we start with; it is just moving around a lot.

### 3.2 Radiative luminosity

By definition, ULXs are suspected to be examples of supercritical accretion. The functional definition of a ULX is an off-nucleus X-ray point source with a luminosity  $L_{\rm X} > 10^{39}$  erg s<sup>-1</sup>. This limit

is chosen because it lies, more or less, at the Eddington limit for a stellar mass object (compare to equation 1), meaning that ULXs either represent normally accreting objects with mass above what is expected for a stellar remnant (possibly an intermediate-mass black hole), or they are stellar remnants apparently emitting above their Eddington limit. We now know that at least some ULXs host neutron stars (i.e. stellar remnants, e.g. Bachetti et al. 2014; Fürst et al. 2016) and suspect others host stellar-mass black holes (Middleton et al. 2013; Cseh et al. 2014; Middleton & King 2017), so we take ULXs as at least one example of a steadily accreting supercritical system to which our results may apply.

Since the defining characteristic of ULXs is that they have apparent isotropic X-ray luminosities at or above the Eddington limit, it is important for us in this study to look at what radiative luminosity we get from each of our simulations and how that luminosity is distributed in space (since we do not expect ULXs to appear ultraluminous from all directions; Begelman, King & Pringle 2006; Middleton et al. 2021).

In Fig. 4, we report the time-averaged radiative luminosity

$$L_{\rm rad}(r,t) = -\int \int \sqrt{-g} R_t^r d\theta d\phi , \qquad (19)$$

integrated over the full  $4\pi$  sr. We report both the outward  $(u_R^r>0)$  and inward  $(u_R^r<0)$  contributions as a function of radius for all three simulations. The inward luminosity is attributable to photons that are trapped within the accreting gas. The net luminosity,  $L_{\rm net}=L_{\rm out}-L_{\rm in}$ , reflects the difference between these two components.

Generally, we find that the overall (outward) radiative luminosity is a few times  $L_{\rm Edd}$ , consistent with expectations for a supercritical accretion disc. However, just as the inward luminosity consists of radiation that is trapped in the accreting gas, some of the outward luminosity may also be trapped in the optically thick wind, some of which is still bound and may fall back to the disc. For this reason, our  $L_{\rm out}$  likely represents an upper limit of what an observer may measure. Also the luminosities in Fig. 4 represent integrals over the complete radial shell, so they are true, total luminosities, and are thus unlikely to match what an observer would infer from any one particular viewing angle.

Another point regarding the radiative luminosity (Fig. 4) is that the net value  $L_{\rm net}$  changes sign between 5 and  $8r_g$  for all of our simulations, with most of the radiation moving towards the black hole inside that radius and away from the black hole outside it. This dip represents the trapping radius  $r_{\rm tr}$  for each of our simulations. We note that this trapping radius is relatively close to the inner edge of the disc, so we conclude that advection is not a prominent source of cooling beyond about  $20r_g$  in our simulations. Also, to be clear, there is still some  $L_{\rm out}$  even inside  $r_{\rm tr}$ , as can be seen in Fig. 4. The point is, though, there is more  $L_{\rm in}$  than  $L_{\rm out}$ , so in terms of cooling the gas, advection is dominant in that region.

An important distinction between optically thick accretion discs and stellar objects is that we do not expect the radiation from discs to be isotropic. Rather, we expect most of it to come out within an optically thin cone centred about the black hole spin axis. Fig. 5 shows that the region around the pole in each case is both relatively evacuated of material and lies outside the effective photosphere of the disc, so is optically thin. We locate the effective photosphere by integrating the quantity  $-(u_t + u_r)\kappa_e\rho$  inwards from the outer radial boundary of the simulation domain along lines of constant  $\theta$  until we reach values > 1, where the effective opacity is  $\kappa_e = \sqrt{0.5\kappa_P^a \kappa^s}$ .

We can also measure how much radiation is escaping at different angles with respect to the black hole spin axis. We show results for this in Fig. 6. Not surprisingly, near the poles, the luminosity is orders

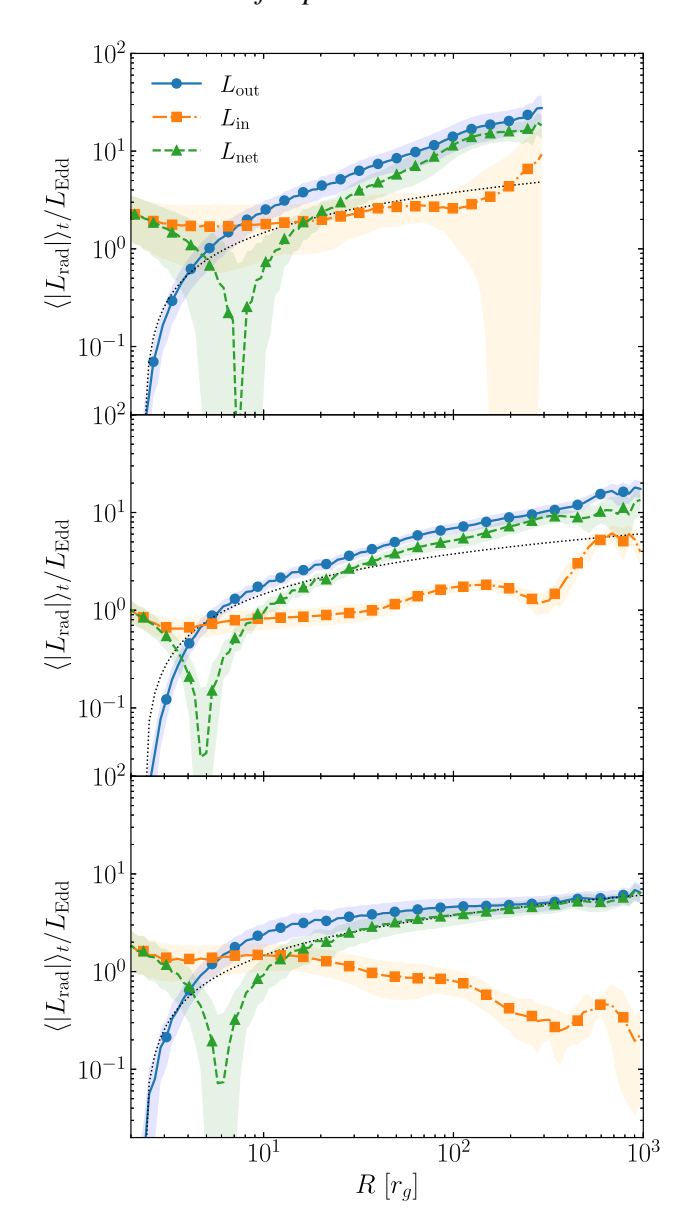


**Figure 4.** Radiative luminosity, both outward  $(L_{\rm out})$  and inward  $(L_{\rm in})$ , as well as the net luminosity  $L_{\rm net} = L_{\rm out} - L_{\rm in}$ , all scaled to Eddington and time averaged from  $t = 50\,000\,t_g$  or  $100\,000\,t_g$  to  $t_{\rm stop}$  for the a9r5 (top), a9r20 (middle), and a9r50 (bottom) simulations. The black dotted curve reports an analytic estimate for  $L_{\rm out}(r) = \ln(r/r_{\rm ISCO})$ . The shaded regions show  $1\sigma$  standard deviations. The trapping radius  $r_{\rm tr}$  is apparent as the sharp dip in  $L_{\rm net}$  around  $r \approx 5r_g$ , where it actually changes sign from inflowing (for  $r < r_{\rm tr}$ ) to outflowing (for  $r > r_{\rm tr}$ ).

of magnitude greater than in the equatorial plane. This provides a simple explanation for why some suspected ULXs, even within our own Galaxy, do not appear to us as such (Begelman et al. 2006; Middleton et al. 2021; Veledina et al. 2024). Interestingly, all of our simulations show very similar  $\theta$  profiles in Fig. 6, meaning they would all appear to be roughly the same luminosity, when viewed from the same inclination. One odd feature, however, is the drop in the radiative flux right along the pole. We note, though, that similar drops have been seen in other numerical studies (e.g. Jiang et al. 2014; Sądowski et al. 2014; Utsumi et al. 2022). In our case, this may have to do with our use of the  $M_1$  closure, although that explanation would not apply to Jiang et al. (2014). Also, the drop is not as pronounced

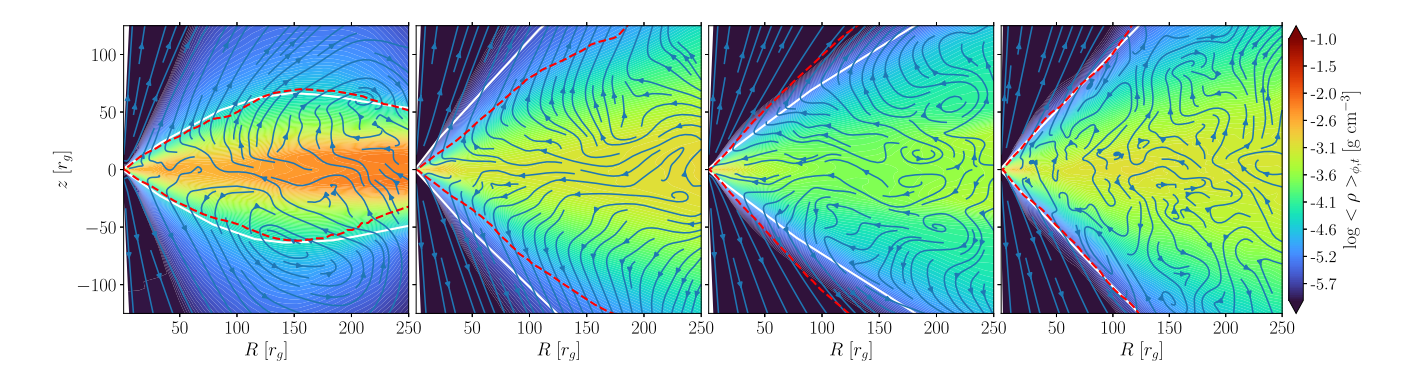
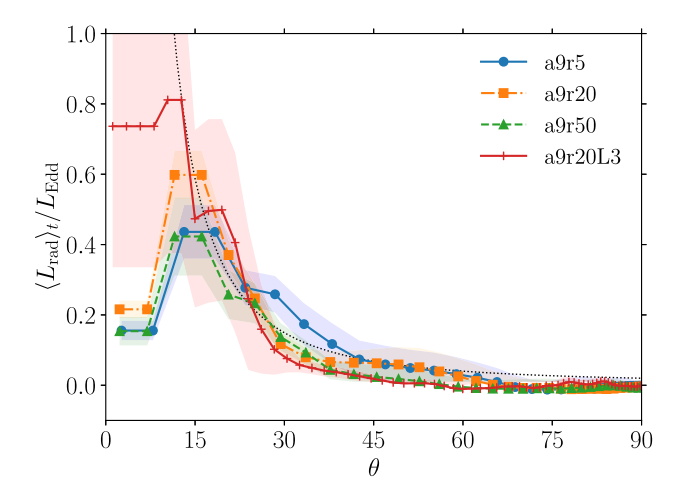


Figure 5. Psueudocolour plot of time- and azimuthally averaged gas density and fluid velocity streamlines for simulations a9r5 (first panel), a9r20 (second panel), a9r50 (third panel), plus the high-resolution extension a9r20L3 (last panel). The white lines represent the effective photospheres, while the red dashed lines delineate the Be = 0 boundaries. Time averaging is over the intervals from  $t = 50\,000\,t_g$ , or 159 000  $t_g$ , or 159 000  $t_g$ , depending on the simulation.



**Figure 6.** Contribution to the radiative luminosity measured at  $r_{\rm eq}$ , broken down into polar angle bins, showing that most of the radiation escapes close to the poles. The black dotted curve suggests  $L_{\rm rad}(\theta) \propto 1/(1-|\cos\theta|)$ . Data are time averaged over the intervals from  $t=50\,000\,t_g$ ,  $100\,000\,t_g$ , or  $159\,000\,t_g$  to  $t_{\rm stop}$ , depending on the simulation, and the shaded regions show  $1\sigma$  standard deviations.

in the high-resolution extension simulation a9r20L3, suggesting this could also be a resolution issue near the pole.

### 3.3 Kinetic luminosity

Some ULXs are accompanied by optical nebulae (e.g. Kaaret, Ward & Zezas 2004) or radio bubbles (e.g. Berghea et al. 2020) with extents of 10–100 pc. These nebulae are thought to be powered by the the ULX itself through some combination of radiation and mass outflow. Indeed, there are now convincing observations of both jets (Middleton et al. 2013; Cseh et al. 2014) and winds (Middleton et al. 2014, 2015; Pinto, Middleton & Fabian 2016; Kosec et al. 2021) from ULXs, with inferred kinetic luminosities on a par with the radiative output. Thus, in addition to radiative luminosities, it is important for us to also examine the kinetic luminosities in the simulations, following

$$L_{\rm kin}(r,t) = -\int \int \sqrt{-g} \rho u^r (u_t + \sqrt{-g_{tt}}) d\theta d\phi . \qquad (20)$$

We do this in Fig. 7, where we compare the time histories of the radiative and kinetic luminosities. Each luminosity is measured at the maximum radius for which each simulation has come into inflow

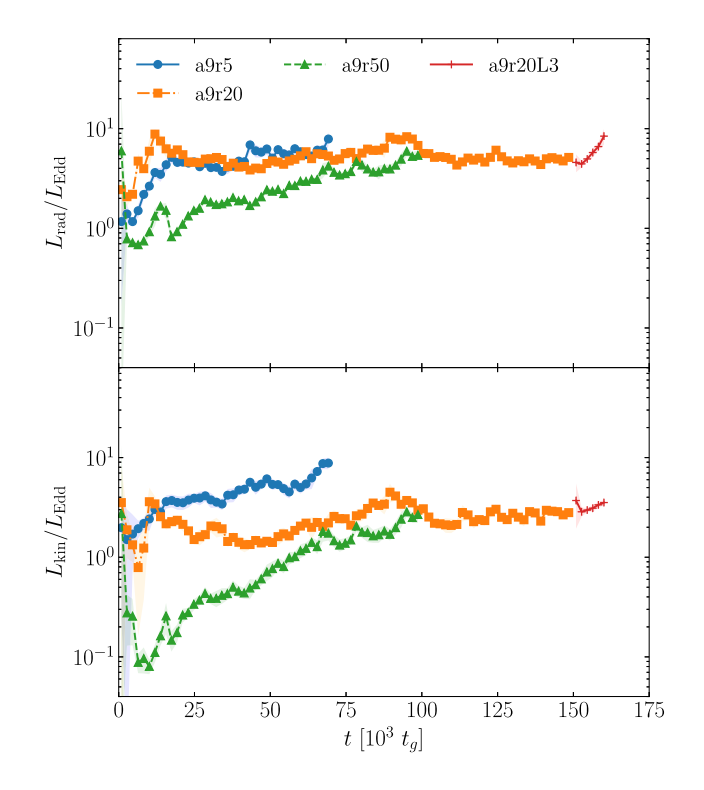


**Figure 7.** Radiative (*top panel*) and kinetic (*bottom panel*) luminosities as a function of time measured at  $r_{\rm eq}$  for each simulation. Data have been smoothed by using a moving boxcar averaging window of 20 consecutive dumps. The shaded regions show  $1\sigma$  standard deviations.

equilibrium,  $r_{\rm eq}$ , based on  $\dot{m}_{\rm net}$  being flat in Fig. 3. The values for  $r_{\rm eq}$ ,  $L_{\rm out}(r_{\rm eq})$ , and  $L_{\rm kin}(r_{\rm eq})$  are reported for each simulation in Table 1.

The kinetic luminosities are smaller than the radiative ones by about a factor of 2 for the a9r20 and a9r50 simulations, but are roughly equal for the a9r5 one. This is consistent with the fact that the a9r5 simulation exhibits mass outflows in Fig. 3 that are significantly stronger than the other simulations.

As mentioned before, we have measured all of our luminosities through the full  $4\pi$  sr, even though some of the outward radiation may be trapped in the bound outflow and potentially fall back to the black hole at larger radii. Notice that in Fig. 5, the Be=0 surface often lies very close to the photosphere, suggesting that most of the radiation passing through the photosphere will escape, while at least some of that within it will remain trapped. Thus, our luminosities

likely represent the upper limits of what could be observed. For this reason, some other groups have chosen to report luminosities only from their optically thin or unbound regions. In that case, all of their radiation is likely to reach an observer; however, it probably represents a lower limit on the total luminosity since some of the radiation in the optically thick wind should eventually escape as well. Thus, current simulations can really only bracket what the observed luminosity should be.

# 4 COMPARISON WITH SUPERCRITICAL DISC MODELS

As mentioned in Section 1, there are two broad classes of supercritical disc models: those based on advective cooling (e.g. slim discs) and those based on radiatively driven outflows (e.g. critical discs). In this section, we attempt to compare our results with these two classes of models to see if our simulations support either one.

One issue we have to settle before we can make such a comparison is what 'input' mass accretion rate to consider. All analytic models of accretion are based on the assumption that the input mass accretion rate at large radii is fixed. However, even though our simulations have run for extended periods, they have not reached a steady state all the way to their outer boundaries. Therefore, it would not make sense to use the  $\dot{m}$  values there as our input mass accretion rates. Likewise, although we started all of our simulations with a target mass accretion rate in mind based on the Shakura-Sunyaev thin-disc model, this  $\dot{m}_0$  was a poor guess at best. We had no way of knowing a priori what the effective viscosity (parametrized by  $\alpha$ ) would be. Not surprisingly, the measured values for  $\dot{m}_{\rm in}$  are quite different, in general, from our target values and are highly radially dependent. Therefore, for the rest of our analysis, we will use as our input mass accretion rate the value of  $\dot{m}_{\rm in}$  measured at  $r_{\rm eq}$ , where again  $r_{\rm eq}$  is the maximum radius out to which the net mass accretion rate has reached a steady value. The measured values for  $\langle \dot{m}_{\rm in}(r_{\rm eq}) \rangle_t$  are reported for each simulation in Table 1.

### 4.1 Slim disc model

The slim-disc model (Abramowicz et al. 1988) assumes that all of the supplied gas reaches the black hole. In other words, the inward mass accretion rate  $\dot{M}_{\rm in}$  is constant as a function of radius and there are no outflows. This is the first sign that our simulations do not agree with this model, as we see significant mass outflow  $\dot{M}_{\rm out}$  and a highly radially dependent  $\dot{M}_{\rm in}$  in Fig. 2.

Because all of the gas ultimately reaches the black hole in the slim disc model, it necessarily requires some of the radiation to also be advected into the black hole to prevent the outward radiation pressure from overwhelming the inward gravitational force. The prediction is that the photon trapping radius should scale with the mass accretion rate such that  $r_{\rm tr} \approx \dot{m}_0 r_{\rm ISCO}$ . Taking our observed value of  $\dot{m}_{\rm in}(r_{\rm eq})$  as the best measure of  $\dot{m}_0$  in our simulations, this would predict a trapping radius of  $r_{\rm tr} \gtrsim 100 r_g$  for the a9r5 and a9r20 simulations, about 20 times further out than what we actually observe in Fig. 4. This is another sign that our simulations do not agree well with the slim-disc model.

Another key difference between the slim disc model and the standard Shakura–Sunyaev one is that, while the Shakura–Sunyaev model assumes a purely Keplerian rotation profile, the slim disc requires most of the disc to be slightly sub-Keplerian, with only a small inner super-Keplerian region (Abramowicz et al. 1988). We, instead, find that our discs all have almost perfectly Keplerian rotation profiles (see Fig. 8).

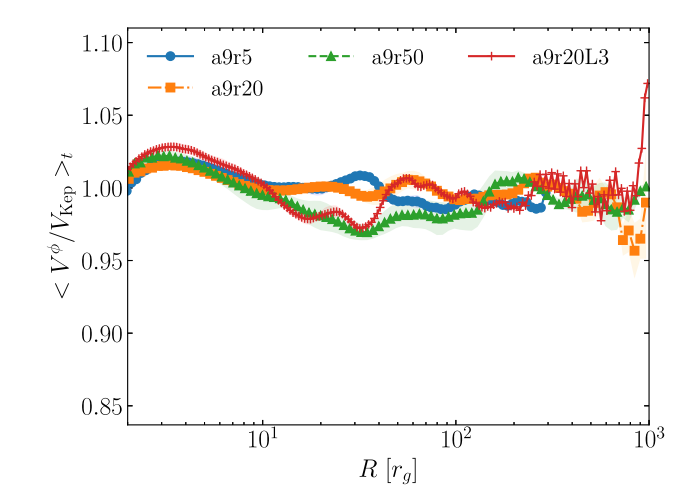


**Figure 8.** Density-weighted time-averaged angular velocity profiles of the discs divided by a purely Keplerian profile. Our profiles differ by no more than a few percent from purely Keplerian. Data are again time averaged over the intervals from  $t = 50\,000\,t_g$ ,  $100\,000\,t_g$ , or  $159\,000\,t_g$  to  $t_{\rm stop}$ , depending on the simulation, and the shaded regions show  $1\sigma$  standard deviations.

### 4.2 Critical disc model

As mentioned previously, the critical disc model (e.g. Fukue 2004) relies on mass outflows to keep the disc below the critical mass accretion rate. Nominally, the outflows should apply to  $r < r_{\rm cr}$ , and it should be the case that  $\dot{m}_{\rm out}(r < r_{\rm cr}) = \dot{m}_{\rm in}(r < r_{\rm cr}) - \dot{m}_{\rm BH}$ . In other words, how much matter goes out must match the excess of what is trying to be fed in minus what is actually making it into the black hole. For  $r_{\rm cr} \gg r_{\rm BH}$ , this implies  $\dot{m}_{\rm out}$  should be quite close to  $\dot{m}_{\rm in}$ , which is exactly what we see in Fig. 2. In fact, the very large variability in  $\dot{m}_{\rm net}$  in Fig. 2 owes to the fact that  $\dot{m}_{\rm in}$  and  $\dot{m}_{\rm out}$  have such close numerical values that the difference between them often changes sign. There is also reasonable quantitative agreement between our accretion profiles and the critical disc model, as Fig. 3 shows that  $\dot{m}_{\rm in}(r)$  closely follows  $[\dot{m}_{\rm in}(r_{\rm cr}) - \dot{m}_{\rm BH}]r/r_{\rm cr}$  (Poutanen et al. 2007).

There are also predictions for how the luminosity should vary for a critical disc inside  $r_{\rm cr}$ . According to Fukue (2004), it should go as  $L(r)/L_{\rm Edd} \propto \ln(r/r_{\rm BH})$ , which actually matches the profiles we find for  $L_{\rm out}$  in Fig. 4 fairly well. Another confirmation is the dependence of  $L_{\rm rad}$  on  $\theta$ . Fig. 6 shows that this agrees with Fukue (2011):  $L(\theta)/L_{\rm Edd} \propto 1/(1-|\cos\theta|)$ , except right at the poles where the simulation data suddenly drop. Finally, the critical disc model predicts that the disc should maintain a nearly Keplerian velocity profile, consistent with what we report in Fig. 8. To conclude, our  $\dot{m}(r)$ , L(r),  $L(\theta)$ , and  $V^{\phi}(r)$  profiles all agree with the predictions of the critical disc model.

# 5 COMPARISON WITH OTHER NUMERICAL WORK

As mentioned in the Introduction, a number of other groups have performed simulations of supercritical accretion discs, and yet, our results appear to be distinct from all previous studies in at least one key aspect: all of our simulations trend towards  $\dot{m}_{\rm BH} \approx 1$ . In other words, our simulations appear to confirm the Eddington limit, whereas other numerical studies do not. In Table 2, we provide a sampling of previous simulation results from a variety of other groups (additionally see table 2 of Toyouchi et al. 2024). Noticeable is that all of those simulations found  $\dot{m}_{\rm BH} \gtrsim 10$ .

## 2828 P. C. Fragile et al.

**Table 2.** Sampling of published supercritical accretion simulation results. We report the input mass accretion rate  $\dot{m}_0$ , the measured  $\dot{m}_{\rm BH}$ , the radiative efficiency  $\eta$ , the ratio of kinetic to radiative luminosities  $L_{\rm kin}/L_{\rm rad}$ , and the ratio of the critical radius to the radius of the torus pressure maximum or the circularization radius of the gas  $r_{\rm cr}/r_{\rm cir}$ . Since most of these simulations used non- or slowly rotating black holes, we assume a radiative efficiency of 10 per cent when defining  $\dot{M}_{\rm Edd}$  in this table. In many cases, we were unable to extract the values of  $\dot{m}_0$  from the information provided in the original paper. In those cases, our estimate of  $r_{\rm cr}$  is based on  $\dot{m}_{\rm BH}$ , which will generally be much smaller than  $\dot{m}_0$ , making our estimates of  $r_{\rm cr}$  stringent lower limits.

| Reference                                      | $\dot{m}_0$ | $\dot{m}_{ m BH}$ | η                       | $L_{ m kin}/L_{ m rad}$ | $r_{\rm cr}/r_{\rm cir}$     |
|--|-------------|-------------------|-------------------------|-------------------------|------------------------------|
| Jiang et al. (2014)                            |             | ~ 22              | 0.045                   | ~ 0.2                   | ≥ 1.5                        |
| Sądowski & Narayan (2016)                      |             | ≥ 10              | $\approx 0.03$          | 0–1.4                   | ≥ 0.4                        |
| Abarca, Kluźniak & Sądowski (2018)             | •••         | 22                | $\approx 0.09$          | ~ 0.1                   | ≥ 0.9                        |
| Utsumi et al. (2022)<br>Yoshioka et al. (2022) | 35–200      | ≥ 10<br>11–38     | 0.003–0.03<br>0.01–0.02 | 0.01–0.4<br>0.02–0.29   | $\geq 0.5$<br>$\gtrsim 0.02$ |

We have a few ideas about why our simulations may have yielded different results:

- (i) Most previous simulations started from a finite torus of gas, and in many of them, the critical radius  $r_{\rm cr}$ , where the radiation pressure first exceeds gravity, lies beyond the pressure maximum of the torus. This may prevent the disc from having the necessary space and time to fully adjust to the radiation pressure before accreting. This was already pointed out in Kitaki et al. (2021).
- (ii) In other cases, it must be that the ratio of the advection time-scale to the radiation diffusion time-scale is much smaller than in our simulations. This could be due to a loss of angular momentum support, leading to significantly sub-Keplerian angular velocity profiles and short advection times in the other simulations. Or the low  $\alpha$  values in our own simulations may lead to unrealistically large advection times.
- (iii) Another possibility is that the radiation diffusion time-scale in the other simulations is much longer, either because of differences between the radiative transport methods or because some of those simulations lack MHD turbulence, which can give the radiation easier channels to escape from the disc.
- (iv) Finally, our unique starting magnetic field topology could also be a contributor. Perhaps some field topologies are more prone to driving Blandford–Payne (Blandford & Payne 1982) winds than others, possibly altering  $\dot{M}_{\rm out}$ , or yield lower saturation values for  $\alpha$ , altering  $\dot{M}_{\rm in}$ .

Since we think our methodology and set-up are more appropriate for simulating large supercritical accretion discs, as may be applicable to ULXs, than any previous simulations, we stand by our finding that such discs are locally Eddington limited at all radii, even when  $m_0 \gg 1$ .

Not surprisingly, since we measure comparable luminosities to previous simulations, but significantly smaller  $\dot{m}_{\rm BH}$ , our discs yield radiative efficiencies that are an order of magnitude or more higher. Using our values for  $L_{\rm out}(r_{\rm eq})$  and  $\dot{M}_{\rm BH}$ , we measure radiative efficiencies of  $\langle \eta \rangle_t = 0.3-0.7$ . This is somewhat higher than the efficiency expected from thin-disc theory (0.156). However, as mentioned in Section 3.2, our values for  $L_{\rm out}$  should be viewed as upper limits, meaning our values for  $\eta$  are also upper limits. To avoid confusion, we remind our readers that our simulations are not done in the magnetically arrested disc limit, which can also result in high radiative efficiencies (Thomsen et al. 2022).

### 6 CONCLUSIONS

We have reported on one of the first sets of large (radially extended) three-dimensional GRRMHD simulations of supercritical accretion

on to black holes. This work is most directly applicable to ULX systems, but may also tell us something about the growth history of black holes over cosmic time.

The most notable finding in our work is that all of our simulations trend towards  $\dot{m}_{\rm BH} \approx 1$ . The takeaway is that for supercritical discs fed by thin Keplerian discs at large radii, it appears  $\dot{M}_{\rm Edd}$  is a meaningful limit,<sup>5</sup> though this should be validated over a wider parameter range. This is in good agreement with long-standing theory, but poses a significant challenge when trying to understand the growth of the first supermassive black holes. Either they cannot grow from steady long-term accretion from a large aligned, Keplerian disc or they cannot start from stellar mass accretors.

To help interpret our results, we tested them against two broad classes of models of supercritical accretion: advection-dominated slim discs and outflow-dominated critical discs. We found that our results do not agree with the main predictions of the slim disc, as we see significant mass outflow, a small trapping radius, and nearly perfectly Keplerian velocity profiles. By contrast, our results agree well with the critical disc model, where mass outflow closely balances mass inflow at all radii to produce a net accretion rate close to  $\dot{M}_{\rm Edd}$ . We also found that our luminosity profiles, both in radius L(r) and polar angle  $L(\theta)$ , match the predictions of the critical disc model.

We caution that it is unclear whether or not we resolve the critical radius  $r_{\rm cr}$  within our computational domain. One way to identify this radius would be to look for where the profile of  $\dot{m}_{\rm in}(r)$  (or likewise  $\dot{m}_{\rm out}(r)$ ) flattens out (i.e. becomes independent of r). Unfortunately, we do not see convincing evidence for such plateaus in Fig. 3 for any of our simulations. This tells us that  $r_{\rm cr}$  must lie beyond the equilibrium radius  $r_{eq}$  achieved in each simulation (see Table 1). It could be that extending these simulations further in time would allow us to eventually capture  $r_{cr}$  on the grid, or it could be that we would need to extend the grid even further out in radius. Alternatively, we could try other disc parameters to see if we could bring  $r_{\rm cr}$  to a smaller radius that is more easily captured. Regardless of how it is accomplished, it is an important goal to try to capture  $r_{cr}$  within the computational domain, and we will continue to work towards that in future simulations. However, this does not alter any of the conclusions we put forth in this study.

Our result of the Eddington limit being enforced in all our simulations is surprising, as it sits in contrast to nearly all previous numerical simulations of supercritical accretion. We speculated in Section 5 that this likely has to do with differences in how we set

<sup>&</sup>lt;sup>5</sup>The Eddington limit does not apply whenever the angular momentum of the gas is so low that it cannot circularize as a disc before it accretes into the black hole (Fragile et al. 2012; Inayoshi, Haiman & Ostriker 2016).

up our simulations compared to all other work. If so, that is an important lesson to consider for anyone thinking of doing simulations of supercritical accretion in the future. One clear point seems to be that if the circularization radius of the gas  $r_{\rm cir}$  is smaller than the critical radius  $r_{cr}$ , then the disc may not be able to adjust fully to the critical solution and will therefore be forced to favour the advective one, as may be appropriate for TDEs but not ULXs.

#### **ACKNOWLEDGEMENTS**

PCF gratefully acknowledges the support of the National Science Foundation through grants PHY-1748958 and AST-1907850 and NASA under award No 80NSSC24K0900, MJM gratefully acknowledges the support of STFC (ST/V001000/1). DAB acknowledges support from IIT-Indore, through a Young Faculty Research Seed Grant (project: 'INSIGHT'; IITI/YFRSG/2024-25/Phase-VII/02). This work was performed in part at the Aspen Center for Physics, which is supported by National Science Foundation grant PHY-1607611. This work used the DiRAC Memory Intensive service (Cosma8) at Durham University, managed by the Institute for Computational Cosmology on behalf of the STFC DiRAC HPC Facility (www.dirac.ac.uk). The DiRAC service at Durham was funded by BEIS, UKRI, and STFC capital funding, Durham University and STFC operations grants. DiRAC is part of the UKRI Digital Research Infrastructure.

### DATA AVAILABILITY

The data underlying this paper will be shared upon reasonable request to the corresponding author.

### REFERENCES

```
Abramowicz M. A., Fragile P. C., 2013, Living Rev. Relativ., 16, 1
Abramowicz M. A., Czerny B., Lasota J. P., Szuszkiewicz E., 1988, ApJ, 332,
   646
Anninos P., Fragile P. C., Salmonson J. D., 2005, ApJ, 635, 723
Asahina Y., Ohsuga K., 2022, ApJ, 929, 93
Bañados E. et al., 2018, Nature, 553, 473
Bachetti M. et al., 2014, Nature, 514, 202
Begelman M. C., Pringle J. E., 2007, MNRAS, 375, 1070
Begelman M. C., King A. R., Pringle J. E., 2006, MNRAS, 370, 399
Beloborodov A. M., 1998, MNRAS, 297, 739
Bennett J. S., Sijacki D., Costa T., Laporte N., Witten C., 2024, MNRAS,
```

Abarca D., Kluźniak W., Sadowski A., 2018, MNRAS, 479, 3936

527, 1033 Berghea C. T., Johnson M. C., Secrest N. J., Dudik R. P., Hennessy G. S., El-khatib A., 2020, ApJ, 896, 117

Blandford R. D., Payne D. G., 1982, MNRAS, 199, 883

Cseh D. et al., 2014, MNRAS, 439, L1

Dai L., McKinney J. C., Roth N., Ramirez-Ruiz E., Miller M. C., 2018, ApJ, 859, L20

Fragile P. C., Gillespie A., Monahan T., Rodriguez M., Anninos P., 2012, ApJS, 201, 9

Fragile P. C., Olejar A., Anninos P., 2014, ApJ, 796, 22

Fragile P. C., Etheridge S. M., Anninos P., Mishra B., Kluźniak W., 2018, ApJ, 857, 1

Fragile P. C., Nemergut D., Shaw P. L., Anninos P., 2019, J. Comput. Phys. X, 2, 100020

```
Fukue J., 2004, PASJ, 56, 569
```

Fukue J., 2011, PASJ, 63, 803

Fürst F. et al., 2016, ApJ, 831, L14

Hawley J. F., Guan X., Krolik J. H., 2011, ApJ, 738, 84

Hawley J. F., Richers S. A., Guan X., Krolik J. H., 2013, ApJ, 772, 102 Hu H., Inayoshi K., Haiman Z., Quataert E., Kuiper R., 2022, ApJ, 934, 132

Inayoshi K., Haiman Z., Ostriker J. P., 2016, MNRAS, 459, 3738

Jiang Y.-F., Stone J. M., Davis S. W., 2013, ApJ, 778, 65

Jiang Y.-F., Stone J. M., Davis S. W., 2014, ApJ, 796, 106

Kaaret P., Ward M. J., Zezas A., 2004, MNRAS, 351, L83

Kaaret P., Feng H., Roberts T. P., 2017, ARA&A, 55, 303

King A. R., Davies M. B., Ward M. J., Fabbiano G., Elvis M., 2001, ApJ, 552, L109

King A., Lasota J.-P., Middleton M., 2023, New Astron. Rev., 96, 101672

Kitaki T., Mineshige S., Ohsuga K., Kawashima T., 2021, PASJ, 73, 450

Kosec P. et al., 2021, MNRAS, 508, 3569

Middleton M. J., King A., 2017, MNRAS, 470, L69

Middleton M. J. et al., 2013, Nature, 493, 187

Middleton M. J., Walton D. J., Roberts T. P., Heil L., 2014, MNRAS, 438, L51

Middleton M. J., Walton D. J., Fabian A., Roberts T. P., Heil L., Pinto C., Anderson G., Sutton A., 2015, MNRAS, 454, 3134

Middleton M. J. et al., 2021, MNRAS, 506, 1045

Middleton M. J., Higginbottom N., Knigge C., Khan N., Wiktorowicz G., 2022, MNRAS, 509, 1119

Mishra B., Fragile P. C., Johnson L. C., Kluźniak W., 2016, MNRAS, 463,

Mishra B., Fragile P. C., Anderson J., Blankenship A., Li H., Nalewajko K., 2022, ApJ, 939, 31

Novikov I. D., Thorne K. S., 1973, in Dewitt C., Dewitt B. S., eds, Black Holes (Les Astres Occlus), Gordon and Breach, New York, p. 343

Ohsuga K., Mori M., Nakamoto T., Mineshige S., 2005, ApJ, 628, 368

Penna R. F., Sadowski A., McKinney J. C., 2012, MNRAS, 420, 684

Pinto C., Middleton M. J., Fabian A. C., 2016, Nature, 533, 64

Poutanen J., Lipunova G., Fabrika S., Butkevich A. G., Abolmasov P., 2007, MNRAS, 377, 1187

Schneider R., Valiante R., Trinca A., Graziani L., Volonteri M., Maiolino R., 2023, MNRAS, 526, 3250

Shakura N. I., Sunyaev R. A., 1973, A&A, 24, 337

Shakura N. I., Sunyaev R. A., 1976, MNRAS, 175, 613

Sądowski A., 2009, ApJS, 183, 171

Sądowski A., 2016, MNRAS, 459, 4397

Sądowski A., Narayan R., 2016, MNRAS, 456, 3929

Sadowski A., Narayan R., Tchekhovskoy A., Zhu Y., 2013, MNRAS, 429, 3533

Sądowski A., Narayan R., McKinney J. C., Tchekhovskoy A., 2014, MNRAS, 439, 503

Takahashi H. R., Mineshige S., Ohsuga K., 2018, ApJ, 853, 45

Thomsen L. L., Kwan T. M., Dai L., Wu S. C., Roth N., Ramirez-Ruiz E., 2022, ApJ, 937, L28

Toyouchi D., Hotokezaka K., Inayoshi K., Kuiper R., 2024, MNRAS, 532,

Utsumi A., Ohsuga K., Takahashi H. R., Asahina Y., 2022, ApJ, 935, 26

Veledina A. et al., 2024, Nat. Astron., 8, 1031

Volonteri M., Rees M. J., 2005, ApJ, 633, 624

Wu S., Coughlin E. R., Nixon C., 2018, MNRAS, 478, 3016

Yang J. et al., 2021, ApJ, 923, 262

Yoshioka S., Mineshige S., Ohsuga K., Kawashima T., Kitaki T., 2022, PASJ, 74, 1378

This paper has been typeset from a TFX/LATFX file prepared by the author.